A grid composite meta-surface absorber with thermal isolation structure for terahertz detection

HAILIANG ZHU,[1] GENGCHEN WANG,[1,*] KAI WANG,[2] GANYU LIU,[1] YUXIN ZHOU,[1] SHENGLIN XIE,[1] YUJIE DI,[1] JIANKAI XU,[1] HUAIREN ZHOU,[1] JINCHAO MOU,[3] AND CAN DING,[4]

[1]*School of Electronics and Information, Northwestern Polytechnical University, Xi'an 710072, Shaanxi, China*
[2]*College of Information Science and Electronic Engineering, Zhejiang University, Hangzhou 310027, Zhejiang, China*
[3]*China Satellite Network Innovation Company Ltd, Beijing 100190, China*
[4]*Globe Big Data Technologies Centre (GBDTC), University of Technology Sydney, Sydney 2007, NSW, Australia*
**wanggc@mail.nwpu.edu.cn*

Abstract: This paper specifically focuses on the absorber, the critical component responsible for the detector's response performance. The meta-surface absorber combines two resonant structures and achieves over 80% absorptance around 210 GHz, resulting in a broad operating frequency range. FR-4 is selected as the dielectric layer to be compatible with standard printed circuit board (PCB) technology, which reduces the overall fabrication time and cost. The absorbing unit and array layout are symmetrically designed, providing stable absorptance performance even under incident waves of different polarization angles. The polarization-insensitive absorptance characteristic further enhances the compatibility between the absorber and the detector in the application scenario. Furthermore, the thermal insulation performance of the absorber is ensured by introducing thermal insulation gaps. After completing fabrication through PCB technology, testing revealed that the absorber maintained excellent absorptance performance within its primary operating frequency range. This performance consistency closely matched the simulation results.

1. Introduction

Terahertz was originally proposed by spectroscopists and is used to describe electromagnetic waves with frequencies below the far-infrared range[1]. With the development of electromagnetism, terahertz receives a more specific definition, referring to the frequency from 0.1 to 10 THz (wavelengths ranging from 0.3 mm to 30 μm)[2]. Plagued by high atmospheric absorptance and non-negligible manufacturing errors, research about terahertz technologies is faltering and there remain significant challenges [3,4]. However, with the development of photonics and nanotechnology, terahertz radiation has gradually demonstrated vast potential applications in various fields[5,6]. Terahertz waves have the advantages of low photon energy[7,8], minimal damage to objects[9,10], unique penetration capabilities[11-14], strong anti-interference ability[5], and the existence of "fingerprint spectra" for certain materials in this frequency range[15-17]. These characteristics make terahertz radiation highly desired in the field of imaging and detection.

Terahertz detection and imaging techniques can be classified into two main categories based on the signal they receive: pulse imaging and continuous-wave imaging. The latter offers advantages such as fast imaging speed, good stability, and high integration[9,18-20]. Thermal detectors based on the opto-thermal effect are a classic approach to achieving continuous-wave imaging and do not need additional cooling equipment. These detectors consist of pixels made of thermally sensitive materials. Each pixel absorbs terahertz radiation dependently when exposed to terahertz waves. The resulting heat causes a change in the

resistance of the thermally sensitive material, which is then converted into an electrical signal that can be read out[21]. By extracting changes in the electrical signal by readout circuits, the detection objective is achieved[22,23].

From the above description, it is obvious that the absorptivity of the detector is crucial for its sensitivity. Unfortunately, most natural materials exhibit low absorptance of terahertz waves[24]. Electromagnetic metamaterials and meta-surfaces provide solutions to overcome the limitations of natural absorptive materials[25,26]. Metamaterials are artificially engineered composite structures, and meta-surfaces are two-dimensional forms of metamaterials[27,28]. Meta-surfaces have shown great application possibilities in the control of spatial beams, polarization detection, sensing, optical imaging, and quantum science[29-31]. By designing the structure, size, and arrangement of meta-surfaces, it is possible to manipulate the electromagnetic parameters of the material and achieve high absorptance in the terahertz range[32-35].In this area of research, there have been a series of reports based on metals and even phase-change materials, greatly expanding the working frequency bands of absorptive structures through the utilization of these materials[36-38].

This paper proposes a meta-surface absorber suitable for terahertz focal plane array detectors, with a thickness of 234μm. The structure adopts the classical "sandwich" model, which consists of a three-layer structure of "metal-dielectric-metal." Typically, such absorbers are manufactured using semiconductor processes, including processes such as magnetron sputtering, photolithography, chemical vapor deposition, etc., which makes them expensive and time-consuming to produce. Therefore, this paper considers using printed circuit board (PCB) technology to fabricate the absorber, significantly reducing financial and time costs. To meet the requirements of PCB technology, FR-4 is employed as the dielectric layer for this absorber. To broaden the absorptance bandwidth, the metal pattern of this meta-surface is composed of two different structures. The shape and arrangement of the units are designed to be centrally symmetric, ensuring stable absorptance performance for incident waves with different linear polarization directions. To enhance the thermal response of the absorber, an overall inter-row spacing is engineered to cut off heat transfer between adjacent rows. After fabrication and measurements, it is found that the most crucial absorptance performance is closely matched to the simulations.

2. Design and characteristics of structures

Absorptance, absorptance bandwidth, and polarization effect are important indicators for evaluating the absorptance performance of an absorber[39]. The polarization effect is used to assess whether the absorber is sensitive to changes in the direction of incident waves, i.e., whether the absorptance curve is affected when the polarization angle of the incident wave changes. Absorptance bandwidth refers to the frequency range over which the absorber exhibits absorptance above a certain threshold value. The ideal scenario for absorbers is to be polarization-insensitive and possess a wide absorptance bandwidth, thereby significantly expanding the application scenarios of absorbers.

In this paper, the design goal of the absorber is to achieve a broader absorptance bandwidth and higher absorptance while maintaining certain dimensions and material composition. Additionally, it should exhibit stable absorptance characteristics when subjected to incident waves with different polarization directions and incident angles. Absorptance is a quantitative measure of the absorber's absorptance capability and can be calculated using the formula below:

$$A(\omega) = 1 - R(\omega) - T(\omega) \tag{1}$$

In this context, $R(\omega)$ and $T(\omega)$ represent reflectance and transmittance, respectively. Achieving a higher absorptance requires reducing the reflection and transmission of the absorber to terahertz waves. In the theory of electromagnetic wave transmission, S-parameters are crucial parameters characterizing electromagnetic wave transmission

properties. If we consider the absorber as a two-port network, S-parameters are typically represented in matrix form. For a two-port network, the S-parameter matrix can be written as:

$$S = \begin{bmatrix} S_{11} & S_{12} \\ S_{21} & S_{22} \end{bmatrix} \tag{2}$$

Here, S_{11} represents the reflection coefficient from port 1 to port 1, S_{12} represents the transmission coefficient from port 1 to port 2, S_{21} represents the transmission coefficient from port 2 to port 1, and S_{22} represents the reflection coefficient from port 2 to port 2.

S-parameters can be used to represent reflectance $R(\omega)$ and transmittance $T(\omega)$:

$$\begin{aligned} R(\omega) &= \left|S_{11}\right|^2 \\ T(\omega) &= \left|S_{21}\right|^2 \end{aligned} \tag{3}$$

Therefore, by controlling S_{11} and S_{21}, it is possible to regulate the absorptance rate. S_{11} represents the reflection coefficient, indicating the degree of impedance matching between the structure and free space; if they are exactly matched, the reflection coefficient is 0. S_{21} is the transmission coefficient, reflecting the extent of terahertz wave transmission, and it is related to the skin depth of the metal baseplate of the absorber. When terahertz waves are incident on the surface of a conductor, they induce a current that exponentially decays with depth, resulting in the propagation of incident electromagnetic waves within the conductor. The skin depth, denoted as δ, represents the effective depth of propagation of incident electromagnetic waves within the structure and is generally defined as the depth at which the electric field strength drops to 1/e of its initial value. When the thickness of the conductor is greater than the skin depth, there will be no transmission of electromagnetic waves, and the transmission coefficient S_{21} is 0. If both S_{11} and S_{21} approximate zero, then the absorptance of the absorber can be considered as 1, and this absorber can be referred to as a "perfect absorber"[40].

The skin depth can be represented as follows:

$$\delta = \frac{1}{\sqrt{\pi f \mu_0 \sigma}} \tag{4}$$

Where: δ is the skin depth. f is the frequency of the incident wave. μ_0 is the vacuum permeability (magnetic constant). σ is the electrical conductivity.

By calculation, in the working frequency range of the absorber, the skin depth of copper is in the range of 142 to 152 nm. In the absorber designed in this paper, a 17μm thick copper plate is used as the reflective backing, which is significantly thicker than the skin depth of terahertz waves inside copper. Therefore, little to no electromagnetic wave transmission is expected to occur and S_{21} is 0. During the design process, efforts are made to minimize S_{11} and S_{21} to achieve close to 100% absorptance.

The basic unit of the proposed meta-surface absorber, as shown in Fig. 1, is a three-layer structure manufactured using printed circuit board technology and the parameters of the absorber are listed in Table 1. From bottom to top, the layers consist of the metal backing, dielectric layer, and metal unit layer. The materials for the metal backing and the metal unit layer are copper (with a conductivity of 5.8×10^7 S/m) and a thickness of t. The metal unit layer consists of a combination of grid and square resonator structures, and this combination allows for the absorptance frequency band to be tailored, achieving multi-frequency absorptance. The material for the dielectric layer is FR-4, with a relative permittivity (ε_r) of 4.44 and a loss tangent ($tan\delta$) of 0.02. Typically, dielectric layers use materials like SiO_2 or Si_3N_4, which require integration with semiconductor processes. In this study, FR-4 is used, enabling the use of printed circuit board (PCB) processes instead of semiconductor processes, which reduces production lead times and fabrication costs.

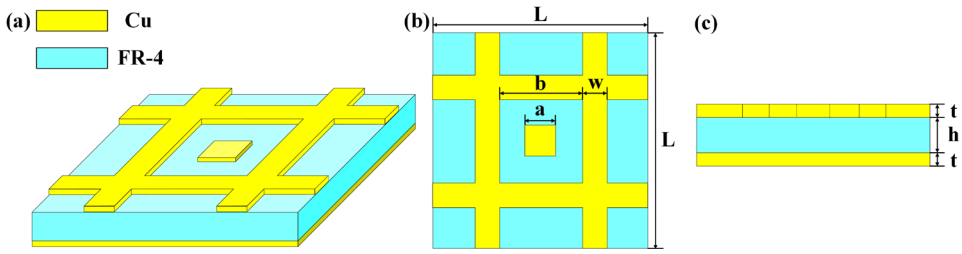

Fig. 1. The (a) perspective view, (b) top view, and (c) side view of the elementary unit cell, symbols a and L represent the square size and unit cell periodicity, respectively; symbols b and w represent the grid size and spacing, respectively; symbols t and h represent the thickness of metal layer and dielectric layer, respectively.

Table 1. The parameters of the absorber

Parameters	**a**	**b**	**w**	**L**	**t**	**h**	**gap**
Value (μm)	**200**	**540**	**160**	**1400**	**17**	**200**	**100**

3. Simulation results and analysis

3.1 Elementary unit cell

Full-wave simulation has been carried out by CST and HFSS to analyze this meta-surface absorber. The primary performance quantification metric for the absorber is absorptance ($A(\omega)$). The absorber designed in this paper exhibits three resonance frequencies, primarily due to the coupling and superposition of two different structures within the metal unit layer. Figure 2 shows the absorptance curve of the absorber. The overall structure achieves nearly 100% perfect absorptance at 220 GHz, with absorptance rates of around 90% at 190 GHz and 206 GHz. Fig. 2 not only presents the absorptance curve for the entire structure but also includes separately simulated absorptance curves for the square and grid structures and a curve representing their superposition for comparison. It can be observed that the superimposed curve closely matches the absorptance curve obtained from the whole-structure simulation, with some frequency-shifting phenomena. The frequency shifts are primarily toward higher frequencies, which is because, with a constant structure thickness, smaller dimensions result in higher resonance frequencies. When two different structures are combined, their absolute dimensions remain unchanged, but their relative dimensions decrease, causing the resonance frequencies to shift higher. Additionally, the coupling between the two structures also contributes to the frequency shifts.

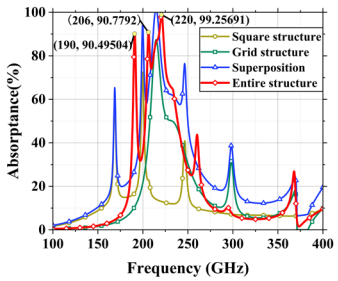

Fig. 2. Simulated absorptance spectra of the unit cell, and three absorptance curves corresponding to three different resonance structures, yellow, green, and blue lines corresponding to square, grid, and superposition of the first two curves, respectively.

Figure 3 displays the surface current distributions on the dielectric surface at 191 GHz, 206 GHz, and 220 GHz. Combining this with Figure 2, it can be observed that at lower frequencies, the surface current primarily concentrates around the small square regions, while at higher frequencies, it predominantly resides around the grid regions. This observation suggests that the small squares influence the low-frequency resonances, while the grids influence the high-frequency resonances. As the frequency increases, the current distribution within the dielectric gradually shifts from the square regions toward the grid regions. This phenomenon can be utilized as a design basis for adjusting resonance frequencies and absorptance, allowing for precise control and optimization of the absorber's performance.

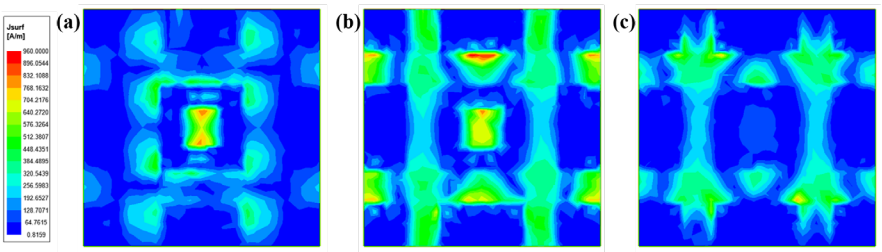

Fig. 3. The surface current distributions on the dielectric surface at (a) 191 GHz, (b) 206 GHz, and (c) 220 GHz.

Analyzing the surface current distribution on both the upper and lower surfaces of the metal unit layer at 220 GHz, as shown in Fig. 4, provides valuable insights into the absorber's behavior. It can be observed that there are both co-directional and counter-directional currents between the two surfaces. The co-directional currents between the two surfaces indicate the presence of electric dipole resonance, while the counter-directional currents suggest the existence of magnetic dipole resonance. These resonances are the underlying mechanisms behind the absorber's absorptance properties. Specifically, at the resonance frequency of 220 GHz, the electric dipole resonance plays a predominant role. This analysis helps in understanding how the absorber interacts with electromagnetic waves at specific frequencies and provides crucial information for designing and optimizing the structure for desired absorptance characteristics.

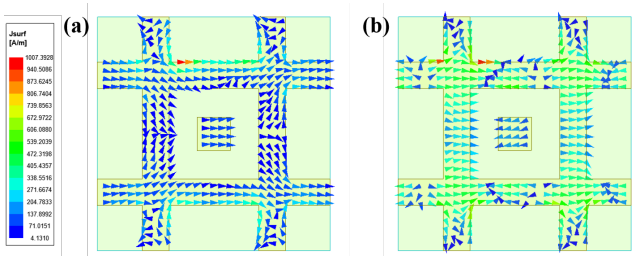

Fig. 4. The surface current distribution on both the (a) upper and (b) lower surfaces of the metal unit layer at 220 GHz.

Furthermore, the absorptance principles of the absorber can be explained from the perspective of impedance matching theory. Similar to the impedance matching theory in the microwave field, when the normalized impedance of the antenna matches the impedance of free space, meaning the real and imaginary parts of both impedances are equal, electromagnetic waves can pass through smoothly without reflection. In this case, it can be considered that the antenna completely absorbs the incident waves. This concept is analogous to the absorptance rate of absorbers. The absorber can be regarded as an antenna, receiving terahertz waves from free space. Therefore, when the impedance of the absorber matches that of free space, there is no reflection along the "transportation route" from free space to the

absorber for terahertz waves. This achieves perfect absorptance of the absorber. Therefore, we can explain the absorptance principle of the absorber through the impedance matching theory. We first extract the normalized complex impedance of the absorber, as shown in the following equation:[41-43]:

$$\tilde{Z}(\omega) = \sqrt{\frac{(1+\tilde{R}(\omega))^2 - \tilde{T}(\omega)^2}{(1-\tilde{R}(\omega))^2 - \tilde{T}(\omega)^2}} \tag{5}$$

In this, $\tilde{R}(\omega)$ and $\tilde{T}(\omega)$ represent the complex reflection coefficient and complex transmission coefficient, respectively. Through the calculation described above, the real and imaginary parts of the normalized complex impedance of the absorber are plotted in Fig. 5(a). Additionally, the impedance curves in the vicinity of the main resonance frequencies are enlarged. Within the range of 190-225 GHz, the real and imaginary parts of the normalized complex impedance of the absorber are in continuous variation, but they are close to 1 and 0, respectively. At the three working frequencies mentioned earlier in the text, the real and imaginary parts are essentially 1 and 0, respectively. This demonstrates that at the resonance frequencies, the absorber is in an impedance-matched state with free space, hence there is minimal generation of reflected waves. Furthermore, the presence of a metal baseplate with a thickness exceeding the skin depth prevents the generation of transmitted waves. These two factors work in conjunction, resulting in the absorptance of a significant portion of the incident energy by the absorber, thereby achieving a higher absorptance rate of the incident waves.

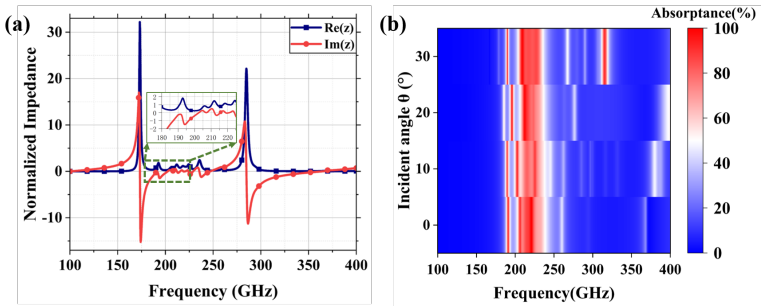

Fig. 5. (a) The normalized impedance of the absorber relative to free space, the inserted picture shows a magnified view of normalized impedance within the absorptance band. (b) The simulated absorptance spectra of different incidence angles, the incidence angle is denoted as θ.

The influence of different incident angles and polarization angles on the absorptance performance is demonstrated below. The incident angle is defined as the angle between the direction of the incident wave and the normal to the meta-surface absorber, which is θ. When the incident angle coincides with the normal, it is defined as 0°. Fig. 5(b) displays the absorptance curves of the absorber under various incident angles. It can be observed that as the incident angle increases to 10°, there are changes in the primary resonance frequency and absorptance, and spikes also appear. When the incident angle further increases to 20°, the changes in the primary resonance frequency and absorptance become smaller compared to the initial state, and there are almost no spikes. However, when the incident angle increases to 30°, the primary resonance frequency and absorptance remain relatively stable compared to the 20° results, but a strong out-of-band resonance peak occurs at 320 GHz. It can be concluded that this structure is highly sensitive to changes in the incident angle. As the incident angle increases, the resonance frequency changes significantly, but the absorptance remains at an acceptable level.

The impact of the polarization angle (denoted as φ) is also analyzed. Due to the strict rotational symmetry of the structure, it is sufficient to perform the simulations of polarization angles from 0° to 45°, and the results are presented in Fig. 6. As the polarization angle gradually increases to 30°, the absorptance at the resonance frequency of 191 GHz remains relatively stable. At the resonance frequency of 206 GHz, the absorptance progressively decreases but remains above 80%. However, a slight deviation in the polarization angle leads to a pronounced dip in the absorptance curve at 220 GHz. With further increasing polarization angles, the distortion of the dip decreases, and it eventually returns to a peak state at around 30°. When the polarization angle reaches 45°, the absorptance curve at 220 GHz remains almost unchanged, but the resonance frequencies in the low-frequency region nearly disappear. This analysis indicates that the high-frequency range of the absorber is sensitive to changes in the polarization angle, while the mid-low frequency range exhibits good polarization insensitivity characteristics.

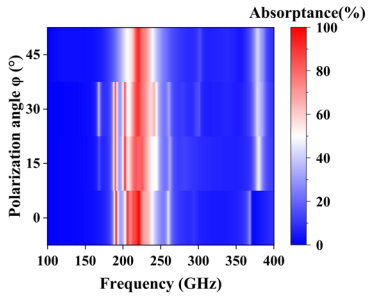

Fig. 6. The simulated absorptance spectra of different polarization angles, the polarization angle is denoted as φ.

3.2 Thermally isolated unit cell

The absorber is a part of the actual detector response module, and it is often combined with micro-cantilevers and other components to form the response module of the detector. The key response parameter for detectors that incorporate micro-cantilevers and absorbers is the heat generated by the absorber. This heat generation is closely related to the absorber's absorptivity, so it's essential to ensure that the absorber has good thermal isolation performance. In addition to the heat generated by the absorber's absorptance coupling, there is also heat transfer between adjacent units. In practical detection scenarios, it's crucial to have good thermal isolation between the individual units. This is because, depending on factors such as the position of the incident wave, the angle of incidence, and polarization, each unit theoretically generates different amounts of heat. The heat readings in different units are used to determine the parameters of the incident wave. Therefore, in this paper, it is planned to introduce gaps between units to create thermal isolation. Due to considerations of structural integrity and feasibility, thermal isolation gaps are introduced only between rows of units. The unit structure with gaps introduced, as well as the simulation results, are shown below:

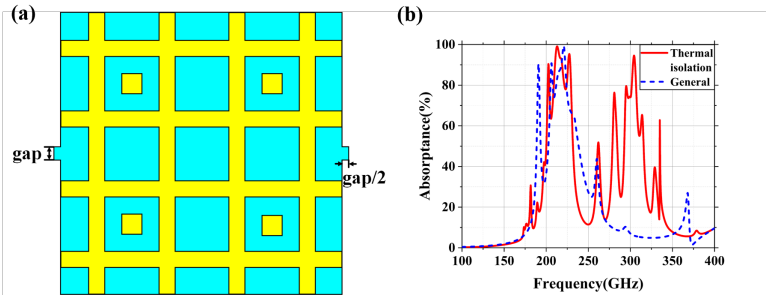

Fig. 7. (a) The top view of a single meta-atom with thermal isolation gaps. (b) Simulated absorptance spectra of two different structures, red solid lines, and blue dash lines correspond to thermal isolation structure and general structure, respectively.

The thermal isolation gaps are connected by columns made of dielectric material, with a thickness equal to that of the dielectric layer, and there is no copper layer covering them either above or below. With the introduction of thermal solation gaps, the absorber still maintains excellent absorptance performance at the original frequency points. However, the introduction of gap structures adds additional resonance frequency points (the appearance of additional high-frequency absorptance peaks), shortens the operating bandwidth, and leads to a significant change in the absorptance spectrum. In COMSOL, electromagnetic-thermal Multiphysics simulations are conducted to observe the differences in electromagnetic-thermal effects between the absorber without gaps and the one with gaps under the same incident wave and thermal environment conditions. In the simulation settings, periodic boundaries are used to simulate an ideal array. The ambient temperature is set at 293.15K, and the convective heat dissipation in the thermal environment is set with a heat transfer coefficient of 5 $W/(m^2 \cdot K)$. With the same incident wave power density, combined simulations of the electromagnetic module and the solid heat transfer module are conducted at 220 GHz. To observe the thermal insulation effect of the thermal isolation gap, we apply incident electromagnetic waves only to the pixel in the top-left corner, while the other pixels do not receive incident waves. This allows us to assess how much thermal impact a heated pixel has on the surrounding pixels. The final results show the temperature distribution on the surface of the absorber, as illustrated in the following figure:

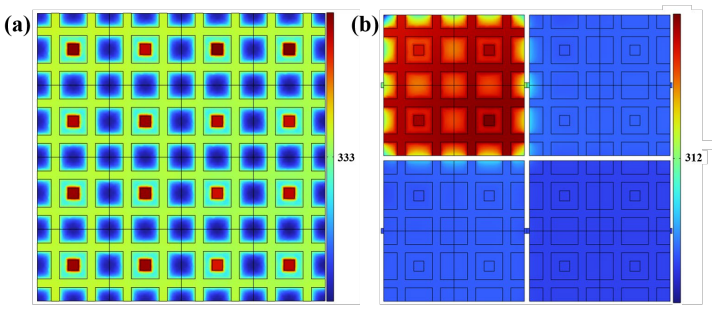

Fig. 8. The temperature distribution on the surface of the (a) general structure and (b) thermal isolation structure.

It can be seen that there are significant differences between these two settings. Compared to the scenario without gaps, the temperature distribution on the pixels in the thermal isolation structure is more uniform, indicating obvious heat transfer between different units. At the same time, within the thermal isolation structure, except for a weak heat transfer phenomenon in the edge areas of the non-heating pixels, the vast majority of the area remains unaffected. The application scenario for this absorptive structure is in thermal detectors, where thermal isolation helps to avoid mutual interference between different pixels, enhancing detection

accuracy. A uniform temperature distribution aids in the rapid acquisition of accurate temperature information by the readout module, thus improving detection response speed. Recently, researchers have applied terahertz absorptive structures in photothermal therapy to eliminate cancer cells. Compared to traditional radiofrequency heating, terahertz waves cause less harm to the human body and exhibit higher eradication rates of cancer cells. Therefore, terahertz absorptive structures considered for their thermal effects hold tremendous development potential in this field[44].

This absorber is designed to exhibit three absorptance peaks, all with high absorptance, and these different resonance frequencies are determined by distinct resonant structures. Additionally, considering the thermal isolation function, gap structures are introduced during physical fabrication to enhance thermal isolation. Simulation results indicate that the absorber with added gap thermal isolation still maintains good absorptive performance at the original resonance frequencies. The structure is sensitive to changes in the incident angle but exhibits good polarization insensitivity. Given its strong practical application potential, we plan to fabricate this structure using PCB technology and conduct relevant tests.

4. Measurements

The absorber is fabricated using PCB technology. The typical PCB fabrication process includes various steps such as layout design, PCB design, board manufacturing, photolithography, etching, component soldering, and assembly. However, for the absorber, the fabrication process is significantly simplified, requiring only PCB design, prototype board production, photolithography, and etching. PCB design, which is equivalent to the absorber's design, has been previously completed during the simulation work. For the prototype board, we use a double-sided FR4-based board with copper layers on both sides. The bottom copper layer remains untreated, serving as the substrate, while the top copper layer is coated with photosensitive resist. A photolithography machine is employed to remove the resist layer, except for the areas corresponding to the resonant structure, creating exposed and unexposed sections. The exposed areas are subsequently etched to remove the copper layer, resulting in the resonant layer of the absorber. A similar photolithography and etching process is applied to the dielectric layer and the bottom substrate to generate gap structures between different units. With these steps completed, the absorber fabrication is finalized, as depicted in Fig. 9(a).

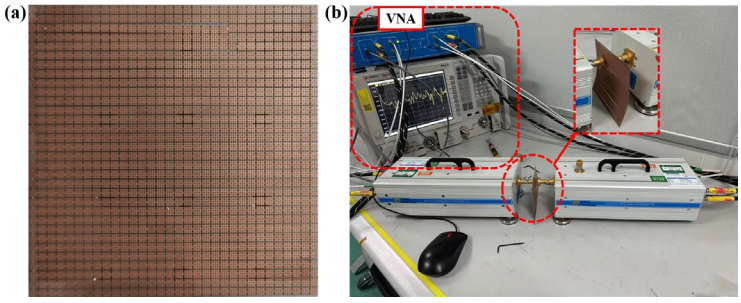

Fig. 9. (a) Image of the meta-surface absorber. (b)The photo of an experimental device, and the magnified view of the absorber.

The most crucial structural parameter for the absorber is absorptance, as discussed earlier. Given that the thickness of the metal backing in this absorber is significantly greater than the skin depth of copper in the working frequency range, there is no transmission occurring. Therefore, the absorptance of the absorber can be obtained by testing the reflection coefficient using a vector network analyzer, as shown in Fig. 9(b).

In Fig. 10, the absorptance test results for the frequency range of 150 GHz to 270 GHz are displayed. The general trend of the test results is similar to the simulation results, with good

alignment at the three resonance frequencies obtafined from the simulation. However, there are some differences in the detailed variations. These variations can be attributed to two main reasons:

First, there is the interference of the electromagnetic environment: The presence of significant electromagnetic interference in the testing environment, especially when not conducted in an anechoic chamber, can affect the accuracy of the measurements. Electromagnetic interference can introduce noise and distort the measured results, potentially causing deviations from simulation data. Second is the dimensional accuracy challenge: The absorber's small dimensions pose challenges in terms of dimensional accuracy during production. While the material selection is well-suited for PCB fabrication, achieving precise dimensions can be challenging. If the spacing between the two metal resonant structures during production is smaller than designed, it can lead to resonance peaks approaching each other, resulting in strong coupling effects. This is a significant factor contributing to the discrepancies between the test and simulation results. These factors highlight the importance of controlled testing environments and precision manufacturing when evaluating and verifying the performance of absorbers.

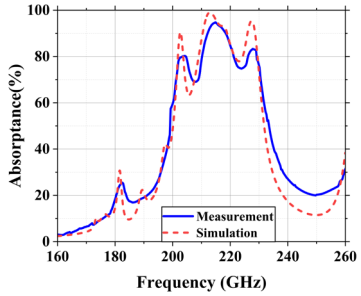

Fig. 10. Measurement of absorber absorptance spectra (blue solid lines), the simulated spectra are plotted in red dash lines for comparison.

5. Conclusion

This paper proposes a grid-based composite terahertz meta-surface absorber using FR-4 dielectric, which achieves multi-frequency absorptance and polarization insensitivity while simplifying the fabrication process. Simulation results indicate that this absorber achieves nearly 100% absorptance at 220 GHz, with absorptances exceeding 80% at 190 GHz and 206 GHz. Although the structure is sensitive to the polarization angle in the high-frequency range and the angle of incidence, it still maintains excellent absorptance performance in the mid-low frequency range when the polarization angle varies within the range of 0 to 30 degrees. This indicates that it is insensitive to polarization. Furthermore, the structure incorporates inter-unit spacing to provide thermal isolation between adjacent units while maintaining absorptive performance. Upon completing fabrication and testing, it is evident that the absorber retains a high level of absorptive performance at its main operating frequencies. This absorber exhibits strong versatility and portability, significantly reducing production lead times and development costs for similar applications. It provides valuable insights for the development of terahertz detectors in the future.

Funding. Natural Science Basic Research Program of Shaanxi (Program No.2022JQ-669)

Disclosures. The authors declare no conflicts of interest.

Data availability. Data underlying the results presented in this paper are not publicly available at this time but may be obtained from the authors upon reasonable request.

References

1. P. H. Siegel, "Terahertz technology," IEEE Trans. Microw. Theory Tech. **50**(3), 910-928 (2002).

2. Y. T. Zhao, B. Wu, B. J. Huang, *et al*., "Switchable broadband terahertz absorber/reflector enabled by hybrid graphene-gold metasurface," Opt. Express **25**(7), 7161-7169 (2017).
3. B. N. Behnken, G. Karunasiri, D. R. Chamberlin, *et al*., "Real-time imaging using a 2.8 THz quantum cascade laser and uncooled infrared microbolometer camera," Opt. Lett. **33**(5), 440-442 (2008).
4. W. L. Chan, J. Deibel, and D. M. Mittleman, "Imaging with terahertz radiation," Rep. Prog. Phys. **70**(8), 1325 (2007).
5. D. Dragoman and M. Dragoman, "Terahertz fields and applications," Prog. Quantum Electron. **28**(1), 1-66 (2004).
6. R. Bogue, "Sensing with terahertz radiation: a review of recent progress," Sens. Rev. **38**(2), 216-222 (2018).
7. R. H. Clothier and N. Bourne, "Effects of THz Exposure on Human Primary Keratinocyte Differentiation and Viability," J. Biol. Phys. **29**(2), 179-185 (2003).
8. S. M. Kim, F. Hatami, J. S. Harris, *et al*., "Biomedical terahertz imaging with a quantum cascade laser," Appl. Phys. Lett. **88**(15), 153903 (2006).
9. M. Nagel, P. Haring Bolivar, M. Brucherseifer, *et al*., "Integrated THz technology for label-free genetic diagnostics," Appl. Phys. Lett. **80**(1), 154-156 (2002).
10. X. Yang, X. Zhao, K. Yang, *et al*., "Biomedical Applications of Terahertz Spectroscopy and Imaging," Trends Biotechnol. **34**(10), 810-824 (2016).
11. T. Zhou, H. Li, W. J. Wan, *et al*., "Terahertz imaging using photomixers based on quantum well photodetectors," AIP Adv. **7**(10), 105215 (2017).
12. J. Bjarnason, T. Chan, A. Lee, *et al*., "Millimeter-wave, terahertz, and mid-infrared transmission through common clothing," Appl. Phys. Lett. **85,** 519-521 (2004).
13. I. O. M. Photonics Technology Letters, Alan, B. Williams, S. Kumar, *et al*., "Real-time imaging using a 4.3-THz quantum cascade laser and a 320 × 240 microbolometer focal-plane array," IEEE Photonics Technol. Lett. **18,** 1415-1417 (2006).
14. B. C. Matthew and J. H. Edwin, "Noninvasive detection of weapons of mass destruction using terahertz radiation," Proc.SPIE **5070,** 38-43 (2003).
15. H.-B. Liu, H. Zhong, N. Karpowicz, *et al*., "Terahertz Spectroscopy and Imaging for Defense and Security Applications," Proc. IEEE **95**(8), 1514-1527 (2007).
16. J. F. Federici, B. Schulkin, F. Huang, *et al*., "THz imaging and sensing for security applications—explosives, weapons and drugs," Semicond. Sci. Technol. **20**(7), S266-S280 (2005).
17. R. Frank, R. Wilk, T. Kleine-Ostmann, *et al*., "Experimental and theoretical study of the THz absorption spectra of selected tripeptides," Proc.SPIE **5727,** 12-19 (2005).
18. B. B. Hu and M. C. Nuss, "Imaging with terahertz waves," Opt. Lett. **20**(16), 1716-1718 (1995).
19. F. Sun, Z. Jiang, and X.-C. Zhang, "Analysis of terahertz pulse measurement with a chirped probe beam," Appl. Phys. Lett. **73**(16), 2233-2235 (1998).
20. Z. Jiang and X.-C. Zhang, "Single-shot spatiotemporal terahertz field imaging," Opt. Lett. **23**(14), 1114-1116 (1998).
21. Y. Cui, Y. He, Y. Jin, *et al*., "Plasmonic and metamaterial structures as electromagnetic absorbers," Laser Photon. Rev. **8**(4), 495-520 (2014).
22. F. Alves, D. Grbovic, B. Kearney, *et al*., "Bi-material terahertz sensors using metamaterial structures," Opt. Express **21**(11), 13256-13271 (2013).
23. Y. Wen, D. Jia, W. Ma, *et al*., "Photomechanical meta-molecule array for real-time terahertz imaging," Microsyst. Nanoeng. **3**(1), 17071 (2017).
24. J. Li, J. Li, C. Zheng, *et al*., "Broadband and tunable terahertz absorption via photogenerated carriers in undoped silicon," Sci. China: Phys., Mech. Astron. **65**(1), 214211 (2021).
25. R. A. Shelby, D. R. Smith, and S. Schultz, "Experimental Verification of a Negative Index of Refraction," Science **292**(5514), 77-79 (2001).
26. J. B. Pendry, A. Holden, D. Robbins, *et al*., "Magnetism from conductors and enhanced nonlinear phenomena," IEEE Trans. Microw. Theory Tech. **47,** 2075-2084 (1999).
27. H. Li, C. Zheng, H. Xu, *et al*., "Diatomic terahertz metasurfaces for arbitrary-to-circular polarization conversion," Nanoscale **14**(35), 12856-12865 (2022).
28. S. Zong, D. Zeng, W. Yuan, *et al*., "Recent advances on perfect light absorbers and their promise for high-performance opto-electronic devices [Invited]," Chin. Opt. Lett. **20**(7), 073603 (2022).
29. J. Li, C. Zheng, J. Li, *et al*., "Polarization-dependent and tunable absorption of terahertz waves based on anisotropic metasurfaces," Opt. Express **29**(3), 3284-3295 (2021).
30. H. Li, S. Duan, C. Zheng, *et al*., "Terahertz all-silicon metasurfaces with off-axis bifocal characteristics for polarization detection," **12**(16), 3359-3371 (2023).
31. H. Li, C. Zheng, S. Duan, *et al*., "Polarization Detection of Terahertz Waves using All-Silicon Metasurfaces with Tightly Focusing Behavior," Laser Photon. Rev. (to be published).
32. H. Tao, N. I. Landy, C. M. Bingham, *et al*., "A metamaterial absorber for the terahertz regime: design, fabrication and characterization," Opt. Express **16**(10), 7181-7188 (2008).
33. D. R. Smith, J. B. Pendry, and M. C. K. Wiltshire, "Metamaterials and Negative Refractive Index," Science **305**(5685), 788-792 (2004).
34. Y. Liu and X. Zhang, "Metamaterials: a new frontier of science and technology," Chem. Soc. Rev. **40**(5), 2494-2507 (2011).

35. F. Yang, Z. Liang, D. Meng, *et al*., "High-quality factor mid-infrared absorber based on all-dielectric metasurfaces," Opt. Express **31**(4), 5747-5756 (2023).
36. Z. Zhang, Q. Xie, L. Guo, *et al*., "Dual-controlled tunable dual-band and ultra-broadband coherent perfect absorber in the THz range," Opt. Express **30**(17), 30832-30844 (2022).
37. D. Zeng, S. Zong, G. Liu, *et al*., "Dynamically electrical/thermal-tunable perfect absorber for a high-performance terahertz modulation," Opt. Express **30**(22), 39736-39746 (2022).
38. Z. Liu, G. Liu, X. Liu, *et al*., "Spatial and frequency-selective optical field coupling absorption in an ultra-thin random metasurface," Opt. Lett. **48**(7), 1586-1589 (2023).
39. Z.-C. Xu, R.-M. Gao, C.-F. Ding, *et al*., "A broadband planar THz metamaterial absorber," Mod. Phys. Lett. B **29**(12), 1550056 (2015).
40. N. I. Landy, S. Sajuyigbe, J. J. Mock, *et al*., "Perfect Metamaterial Absorber," Phys. Rev. Lett. **100,** 207402 (2008).
41. X. Chen, T. M. Grzegorczyk, B.-I. Wu, *et al*., "Robust method to retrieve the constitutive effective parameters of metamaterials," Phys. Rev. E **70**(1), 016608 (2004).
42. Y. Wen, W. Ma, J. Bailey, *et al*., "Broadband Terahertz Metamaterial Absorber Based on Asymmetric Resonators With Perfect Absorption," IEEE Trans. Terahertz Sci. Technol. **5**(3), 406-411 (2015).
43. D. R. Smith, D. C. Vier, T. Koschny, *et al*., "Electromagnetic parameter retrieval from inhomogeneous metamaterials," Phys. Rev. E **71**(3), 036617 (2005).
44. S. Li, W. Tan, X. Liu, *et al*., "Efficient photothermal therapy with spatially localized high-temperature generation by refractory absorber," Appl. Phys. Lett. **123**(13), 131701 (2023).